Monitoring viscosity changes from time-lapse seismic attenuation: case study from a heavy oil reservoir

Andrey H. Shabelansky*, Alison Malcolm and Michael Fehler

Earth Resources Laboratory, Department of Earth, Atmospheric and Planetary Sciences, Massachusetts Institute of Technology, 77 Massachusetts Ave., Cambridge, MA 02139 USA

ABSTRACT

Heating heavy oil reservoirs is a common method for reducing the high viscosity of heavy oil and thus increasing the recovery factor. Monitoring of these viscosity changes in the reservoir is essential for delineating the heated region and controlling production. In this study, we present an approach for estimating viscosity changes in a heavy oil reservoir. The approach consists of three steps: measuring seismic wave attenuation between reflections from above and below the reservoir, constructing time-lapse Q and Q^{-1} factor maps, and interpreting these maps using Kelvin–Voigt and Maxwell viscoelastic models. We use a 4D relative spectrum method to measure changes in attenuation. The method is tested with synthetic seismic data that are noise free and data with additive Gaussian noise to show the robustness and the accuracy of the estimates of the Q-factor. The results of the application of the method to a field data set exhibit alignment of high attenuation zones along the steam-injection wells, and indicate that temperature dependent viscosity changes in the heavy oil reservoir can be explained by the Kelvin–Voigt model.

INTRODUCTION

In recent years conventional crude oil reservoirs have been in decline, and heavy oil is becoming an important potential resource. The production of conventional cold heavy oil at depths between 50 m and 1000 m has a typical recovery factor of 5% to 10% (Clark 2007). One method to increase recovery is to heat a reservoir to above 200°C either by combustion of part of the heavy oil (Vendati and Sen 2009; Kendall 2009) or by injecting steam into the reservoir (e.g., Clark 2007). Experimental studies indicate that the properties of heavy oil are strongly temperature dependent. Eastwood (1993) showed that the viscosity of heavy oil drops approximately double logarithmically with increasing temperature between 20°C and 200°C (i.e. $\eta \propto -\log(\log(T))$, where η is viscosity and T is temperature). Mochinaga (2006) showed that the density of heavy oil decreases linearly with increasing temperature. Batzle, Hoffman, and Han (2006a) illustrated

that waves propagating through heavy oil within the ultrasonic frequency band are highly attenuated at higher temperatures than those propagating at lower temperatures. However, the properties of heavy oil are also dependent on frequency. Schmitt (1999) showed with borehole measurements in different frequency bands (vertical seismic profiles (VSP) and sonic) that heavy oil has frequency-dependent velocities even at constant temperature. Empirical studies (e.g., Batzle et al. 2006a; Han, Liu, and Batzle 2007; Behura et al. 2007) showed that the shear modulus of heavy oil can in general be predicted by a frequency-dependent Cole–Cole visco-elastic model (Cole and Cole 1941), which has both real and imaginary attenuative parts. In addition to the temperature- and frequency-dependent shear moduli, two parameters control the behavior of the Cole–Cole model. The first is the relaxation frequency that is the frequency where the strongest attenuation is observed and that is related to the temperature through the viscosity of the oil (e.g., Behura et al. 2007). The second is the relaxation coefficient (sometimes called a spread factor) that is the parameter that controls the distribution of the

---
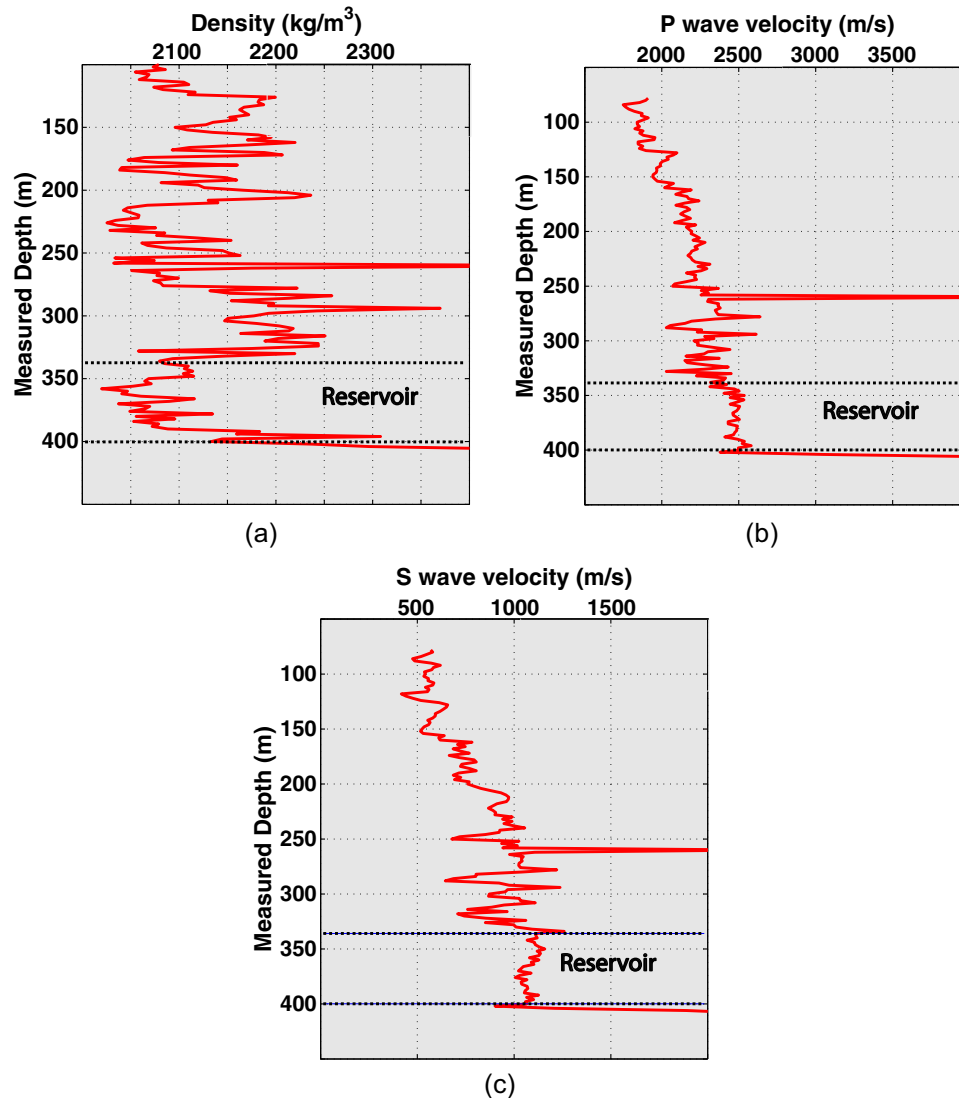
*E-mail: andreys@mit.edu

Figure 1 (a) density, (b) sonic P-wave velocity, and (c) sonic S-wave velocity from well logs from a heavy oil field in Athabasca, Canada. The well logs were measured before the steam was injected into the reservoir.

relaxation frequencies, and that depends primarily on composition (e.g., Han *et al.* 2007). During laboratory experiments at intermediate temperatures between 40°C and 120°C, the peak attenuation is found to be within the seismic frequency band. This means that seismic measurements are ideal for estimating the attenuation response of a reservoir at the intermediate temperatures.

The measurement of seismic attenuation in the field is, in general, a difficult task because of the difficulty in discriminating between the decay of the signal from attenuation and that from geometrical spreading or scattering. The spectral ratio method is a common technique to estimate the attenuation

(Q - factor) of the medium. It separates the effect of attenuation from geometric spreading and is first presented for laboratory measurements of rocks by Toksöz *et al.* (1979) and adjusted for VSP and surface seismic in many studies (e.g., Hauge 1981; Badri and Mooney, 1987 Feustel and Young 1994; Chen and Sidney 1997; Dasgupta and Clark 1998; Sun and Castagna 2000; Hedlin Mewhort and Margrave 2001; Mateeva 2003; Wang 2003; Carter 2003; Vasconcelos and Jenner 2005; Matsushima 2006; Rickett 2006; Lecerf, Rogers, and Lefeuvre 2006; Reine, Clark, and van Der Baan 2009; Clark *et al.* 2009; Blanchard *et al.*, 2009; Reine *et al.* 2012a,b). Note that, for surface seismic data, near surface effects make

the measurements of attenuation even more difficult and less reliable. However, the advent of time lapse surface seismic acquisitions using permanent systems with fixed positions for sources and receivers in heavy oil fields (Byerley *et al.* 2008) has made it possible to obtain high-quality repeatable surface data sets for estimating target-oriented time-lapse attenuation. Using such data, we adapt the standard spectral ratio method so that it can be applied to time-lapse surface reflection seismic data, and we show that changes in seismic attenuation due to the effect of steam injection can be monitored using this method. This paper is divided into four sections. In the first section we review the reservoir properties and time-lapse reflection seismic data set from a heavy oil field in Athabasca, Canada. In the second section, we present the 4D relative spectrum method (4DRSM) and test its robustness and accuracy with a simple two-reflector synthetic model. In the third section we present results obtained by applying this method to a time-lapse data set collected to monitor steam injection in a heavy oil reservoir. Finally, in the fourth section, we show an interpretation of these results using viscoelastic models.

RESERVOIR PROPERTIES AND FIELD SEISMIC DATA

The heavy oil reservoir investigated in this study is located within the McMurray formation of the Manville Group, which overlies the eroded pre-Cretaceous Devonian unconformity surface of carbonates (limestones), and is overlain by the shale-dominant Colorado Group (Barson 2001). The approximate depth of the reservoir is between 340 m and 400 m (see well logs in Fig. 1). Its thickness is between 30 m and 70 m within layers of unconsolidated sands. The initial *in-situ* temperature is 10°–13°C, porosity is in the range of 0.3 to 0.35, and the permeability is above 1 Darcy (Byerley *et al.* 2008). The density and P and S wave velocities within the reservoir are respectively about 2050 kg/m^3, 2500 m/s, and 1100 m/s (Fig. 1), whereas those of the limestone layer, located below the reservoir, typically have much higher values of above 2200 kg/m^3, 3500 m/s, and 1500 m/s, respectively (e.g., Chopra 2010, p. 228). The typical viscosity of heavy oil from the reservoir is between 1000 Pa·s and 5000 Pa·s, and its density is within the range of 8° to 10° API gravity units (Byerley *et al.* 2008). To reduce the viscosity and increase mobility of the heavy oil in the reservoir the steam-assisted gravity drainage (SAGD) method was employed for three months using horizontal wells with continual injection of steam at a temperature of up to 230°C (Clark 2007).
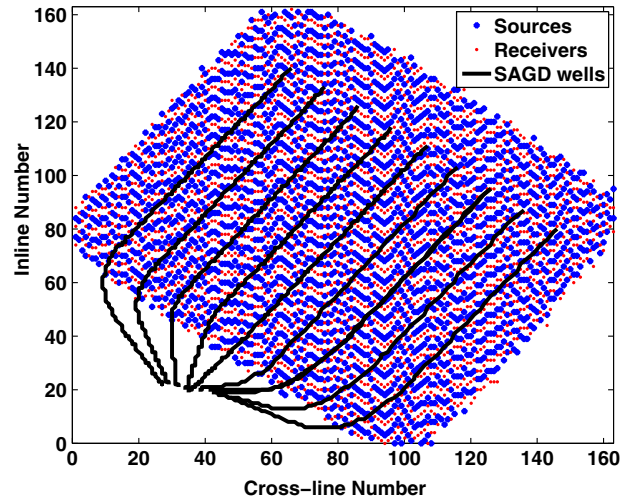

Figure 2 The geometry of the time-lapse surface seismic acquisition for monitoring injected steam. The injection (SAGD) wells are shown as projected from the reservoir depth to the surface. The area of the acquisition is 1600 m × 1600 m with interval of 10 m between in-lines and cross-lines.
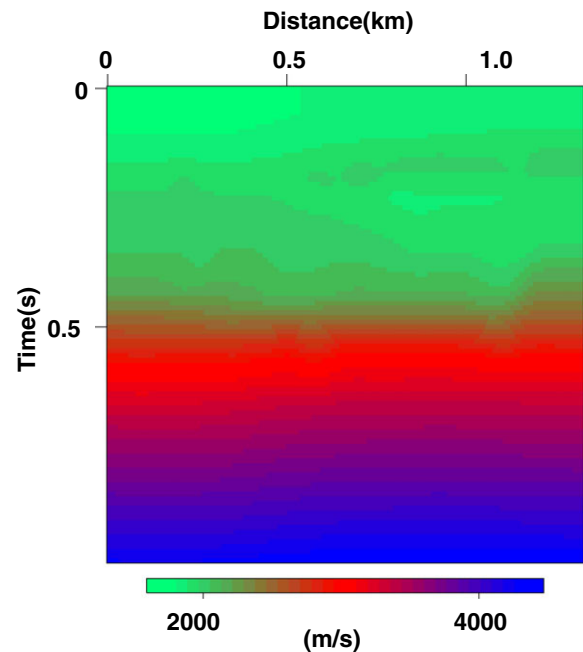

Figure 3 RMS velocity model that was used for migrating both the baseline and monitor seismic data sets. (The zone of the reservoir corresponds to 0.33–0.4 s)

The monitoring of the steam injection is done with a time-lapse surface seismic acquisition using permanent systems with fixed positions for sources and receivers (see Fig. 2) at a depth of 6 m to minimize the effect of
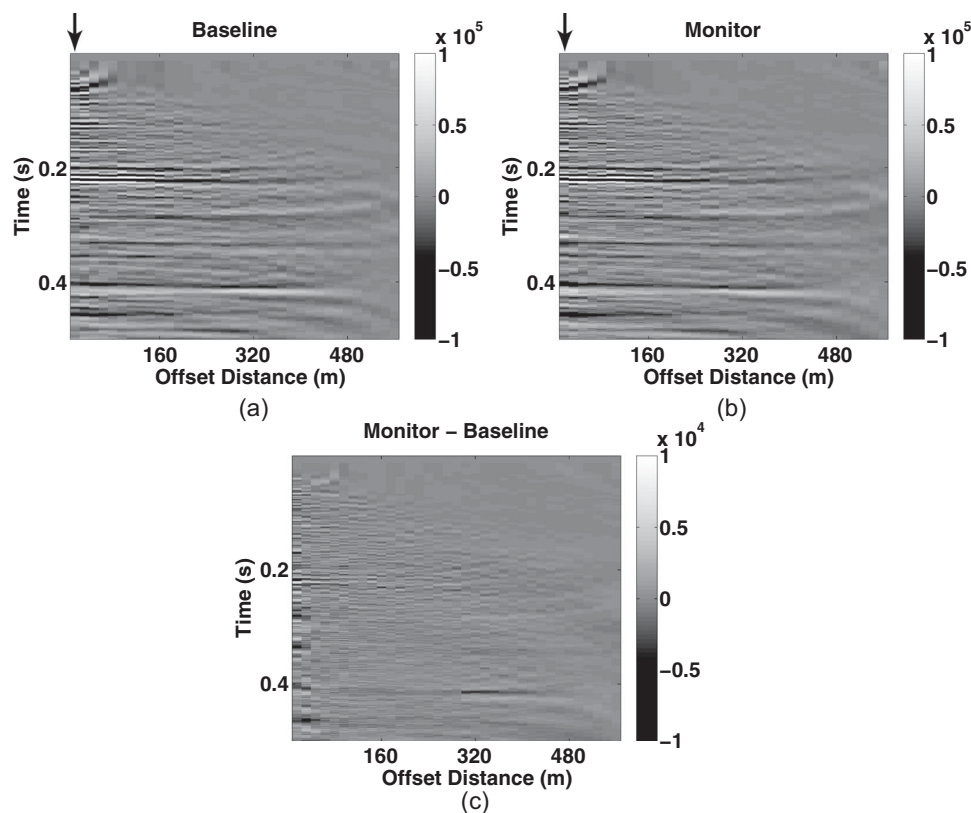
Figure 4 Pre-stack time migrated gathers: (a) baseline, (b) monitor, and (c) their difference for inline 94 and cross-line 64 in Fig. 2. The offset step is 16 m. The arrows in (a) and (b) correspond to the traces whose spectra are shown in Fig. 5 and are shown as wiggle traces in Fig. 8. Note that the amplitude scale of the difference section is one order of magnitude smaller than those of the baseline and monitor sections, and even at this scale, it is difficult to detect the effect of the steam injection.

near-surface variations on signal repeatability. We refer to data collected before the steam injection as the baseline and to that after the injection as the monitor. The total area of the acquisition is 1600 m × 1600 m, with spatial and time sampling of $dx = dy = 10$ m, $dt = 1$ ms, respectively. The RMS velocity model (Fig. 3), estimated with standard velocity analysis, was used to image both the baseline and the monitor data sets because it is difficult to estimate any changes in RMS velocities between the two data sets (Dubucq, D., 2009: personal communication). The time-migrated gathers and their difference (Fig. 4) show the repeatability of the data, illustrated by the flat events in both the baseline and the monitor gathers, and consistent frequency spectra (shown for an entire trace in Fig. 5). The repeatability of the time-lapse data sets was measured using the normalized root mean square (NRMS) differences (Kragh and Christie 2002); most values are between 0.15 and 0.2, which indicate exceptionally good repeatability for land time-lapse data. We attempted to apply 4D matching filters to the data. However, the data after fil-

tering showed less coherence and higher NRMS values, due primarily to the water-level effect. Thus, the baseline and monitor data were only rotated to zero-phase without applying 4D matching between the surveys. After stacking the gathers and producing a 2D stacked section, we observe changes in reflectivity in the vicinity of the reservoir (see the zoomed and magnified regions marked within the windows in Fig. 6 that corresponds to 0.33–0.42 s). In Fig. 7, we also examine amplitude differences and time-shifts between the data sets. Amplitude differences are calculated by differencing the maximum amplitudes within the time window of size 0.01 s centred at time 0.39 s, and time-shifts are obtained by cross-correlation of data within the same window (the region of the reservoir). Although the amplitude differences (Fig. 7(a)) illustrate visible alignment along the SAGD wells, it is difficult to reach the same conclusion from the time-shifts (Fig. 7(b)).

In order to understand the changes in Figs. 6 and 7(a) and to verify that those changes are associated with the steam injection and are not noise, we extracted amplitudes from a
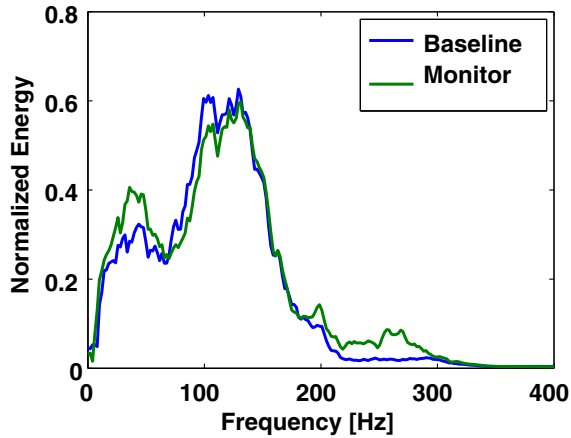
Figure 5 A representative spectrum of the baseline and the monitor traces that correspond to an offset of 16 m in the pre-stack time-migrated gather at inline 94 and cross-line 64 (see the arrow marks in Fig. 4(a) and (b)).

pre-stack time-migrated trace in windows centered at times t_1 and t_2 (see Fig. 8), and separately calculated their spectra. The window around time t_1 corresponds to the region above the reservoir (the portion of the signal that is not affected by the steam injection), whereas that around t_2 is attributed to the region below the reservoir (the portion of the signal that is considered most affected by the steam injection). We observe in Fig. 9 that the spectra above the reservoir are almost the same for both the baseline and the monitor, whereas the spectra that correspond to the region below the reservoir are different between the baseline and the monitor. The main difference in spectra of t_2 (green lines) is observed between 60 Hz and 130 Hz.

Observing the differences in spectra (between the baseline and monitor data sets) that correspond only to the region of the reservoir and knowing that heavy oils are strongly attenuative at intermediate temperatures encourage us to evaluate spectral ratios as a means to quantify attenuation. We calculate the logarithm of the spectral ratio between amplitudes measured at t_2 and t_1 individually for each data set. In Fig. 10, we observe that the logarithm of the spectral ratio for each data set has a fairly linear behavior for frequencies between 15 and 200 Hz (green fit to the blue data points). We interpret this observation to mean that the attenuation of this heavy oil within this seismic frequency range has a constant or nearly constant Q-factor. This can be explained by the fact that the frequency bandwidth of our measurements is very narrow, making the frequency variations of Q difficult to detect. Therefore, to estimate the attenuation caused by the

steam injection, we use a 4D relative spectrum method using a constant Q as a function of frequency, as described in the next section.

4D-RELATIVE SPECTRUM METHOD

In this section we review a time-lapse relative spectrum method (4DRSM) for seismic wave attenuation estimation, which is an adaptation of the spectral ratio method (Toksöz *et al.* 1979) to surface reflection seismic data. We calculate the relative spectra for baseline and monitor surveys separately and take their difference in Q and Q^{-1} to estimate the relative change of the reservoir properties. Thus for the rest of this section, we will describe how to estimate Q of the reservoir only for a single survey.

The method is derived similarly to that of Dasgupta and Clark (1998), Wang (2003), Lecerf *et al.* (2006), and Blanchard *et al.* (2009) by assuming a propagating wave whose amplitude as a function of frequency and depth is given by

$$A(z, f) = G(z) A_0(f) e^{-\alpha(f)z} e^{i(2\pi ft - kz)}, \quad (1)$$

with magnitude

$$|A(z, f)| = G(z) A_0(f) e^{-\alpha(f)z}, \quad (2)$$

where f is the frequency, z is the depth, k is the wavenumber, t is time, $A_0(f)$ is the input source amplitude, $A(z, f)$ is the amplitude of the recorded signal as a function of frequency and depth, $G(z)$ is the geometrical spreading factor (assumed to be real as is standard in seismic processing), and $\alpha(f)$ is the frequency-dependent attenuation coefficient.

By assuming that the attenuation $\alpha(f)$ is a linear function of frequency, we write

$$\alpha(f) = \tilde{\gamma} f \quad \text{or} \quad \alpha(f)z = \gamma f, \quad (3)$$

where

$$\gamma = \tilde{\gamma} z = \frac{\pi}{Qc} z, \quad (4)$$

or

$$\gamma = \frac{\pi t}{Q}, \quad (5)$$

where Q and c are assumed the frequency-independent Q-factor and velocity, respectively.

Substituting equation (3) into equation (2) and changing variables from z to t using the velocity c, we obtain

$$|A(t, f)| = G(t) A_0(f) e^{-\gamma f}. \quad (6)$$

Next, by taking the ratio between the magnitudes of two time windows on the trace (A_1 and A_2), which correspond
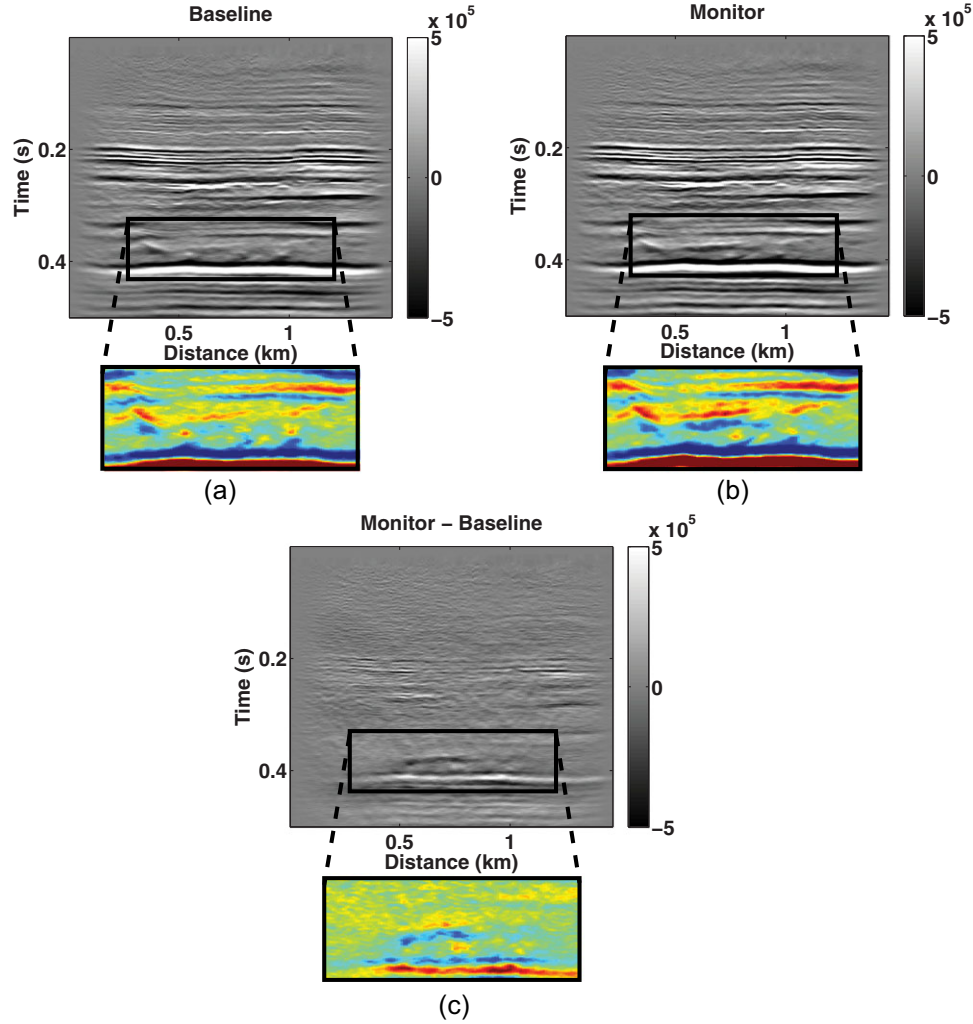
Figure 6 Top: Pre-stack time-migrated stack sections: (a) baseline, (b) monitor, and (c) their difference at inline 94. (The vertical time axis is exaggerated by 2.5 times in comparison to the horizontal distance when converted to depth). Bottom: The zoom panel shows the reservoir interval (0.33-0.42 s); the amplitude of each panel is scaled by the same factor. The observed difference in (c) corresponds to the effect of the steam injection.

to times t_1 and t_2 (Fig. 8), and applying the logarithm, we obtain a linear relation between the log of the spectral ratios and frequency

$$\log\left(\frac{|A_2|}{|A_1|}\right) = -(\gamma_2 - \gamma_1)f + \log\left(\frac{G_2}{G_1}\right), \tag{7}$$

where $(\gamma_1 - \gamma_2)$ and $\log\left(\frac{G_2}{G_1}\right)$ are the slope and intercept, respectively. To avoid dividing by zero, we add a small number to $|A_1|$. At least two methods have been suggested to estimate the slope: a linear least squares fitting as in Toksöz *et al.* (1979) or taking the derivative of the logarithm of the spectral ratio with respect to frequency as in, e.g., Menke, Levin, and Sethi, (1995). Although the latter approach is faster and easier

to apply, our evaluations showed that the former approach is more robust to outliers in the data and was thus used in this study.

From estimates of $\log\left(\frac{|A_2|}{|A_1|}\right)$, we calculate the relative Q-factor, derived in Appendix and which is slightly different from Dasgupta and Clark (1998), as

$$\tilde{Q} = \frac{1}{2}\frac{\pi(t_2 - t_1)}{(\gamma_2 - \gamma_1)}, \tag{8}$$

where $\tilde{Q}$ corresponds to an estimate of the Q-factor for the region between t_1 and t_2. We will denote $\tilde{Q}$ as Q for the rest of of this paper. Note that the factor $\frac{1}{2}$ is added to equation (8) to account for the two-way travel time (see Appendix for more
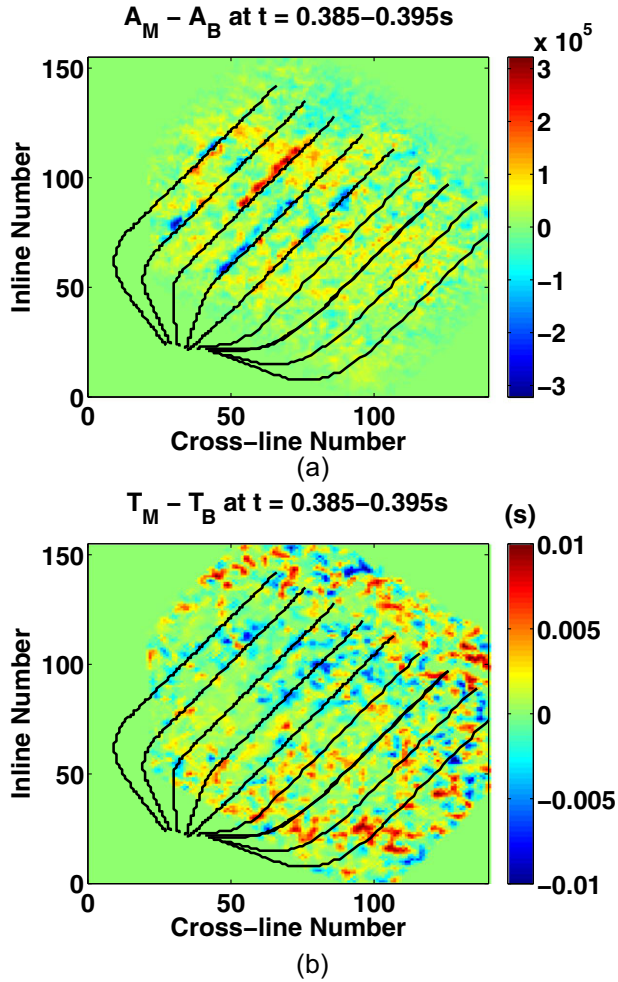
(a)

(b)

Figure 7 Time lapse difference section between the monitor and baseline surveys for (a) amplitude and (b) time, calculated by differencing the maximum amplitudes between 0.385 s and 0.395 s (within the reservoir).

Figure 8 Representative traces from the baseline and monitor surveys for the relative spectrum method that were extracted from the pre-stack time-migrated gather at inline 94, cross-line 64 and offset 16 m (see arrows in Fig. 4(a) and (b)). The window around t_1 corresponds to the region which is not affected by the steam, whereas the window around t_2 corresponds to the steam-affected region.

details). Also note that the geometric factor G corresponds to the intercept and does not affect the estimate of the Q-factor.

4DRSM estimates attenuation between t_1 and t_2 in each survey separately and does not require the attenuation above the reservoir, γ_1, to be the same between the two surveys as in Lecerf *et al.* (2006). In our analysis we thus do not require precise balancing of the amplitude (and spectrum) between the baseline and the monitor traces as the balancing filter cancels during the relative ratio estimation (i.e., $\log(\frac{\|A_2 F\|}{\|A_1 F\|}) = \log(\frac{\|A_2\|}{\|A_1\|})$, where F is the balancing filter between the baseline and monitor traces). This is a strength of the method for time-lapse processing. Thus, the surface related effects between the two surveys are removed during the analysis. Note however that 4DRSM is valid for zero- or near-offsets
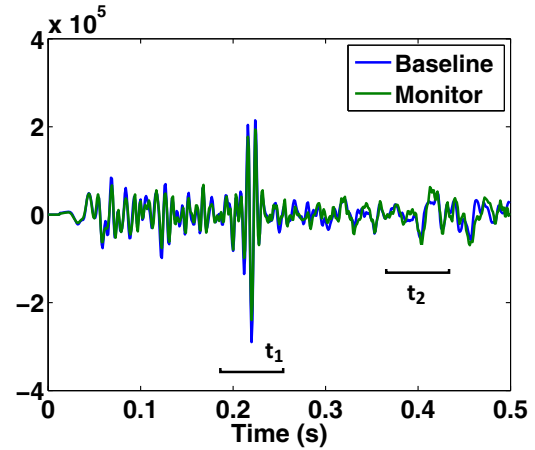
with fairly horizontal structure as it assumes that reflections at t_1 and t_2 have the same propagation path (i.e., a wave propagating from a source to a receiver samples first the reflector above the reservoir and then the reflector below the reservoir).

Workflow

The workflow of the 4DRSM is summarized by the following steps.

For each data set (Baseline or Monitor):

(**i**) Choose a zero- or near-offset trace from each pre-stack time-migrated gather in both data sets.

(**ii**) Extract amplitudes within the windows at times t_1 and t_2.

(**iii**) Calculate the amplitude spectrum for each time window.

(**iv**) Calculate the ratio between spectra and take the logarithm.

(**v**) Fit the data as a function of frequency, and estimate the slope and the error-bar (the difference between the maximum and the minimum possible slopes with 95% confidence).

(**vi**) Calculate Q^{-1} from the slope using equation 8 for each survey separately.

(**vii**) Calculate $\Delta(Q^{-1}) = Q_B^{-1} - Q_M^{-1}$ and $\Delta Q = Q_M - Q_B$, where the subscripts B and M refer to the baseline and monitor data sets, respectively.
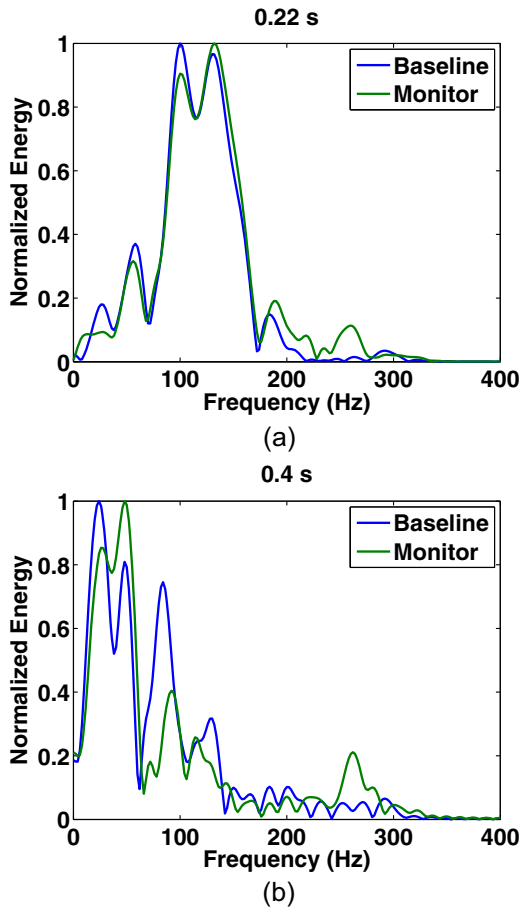
Figure 9 The spectra within the windows at times (a) $t_1 = 0.22$ s (above the reservoir) and (b) $t_2 = 0.4$ s (below the reservoir) of the baseline and monitor traces. The main difference in spectra of t_2 is observed between 60 and 130 Hz, and the frequency bandwidth used for the inversion is between 15 and 200 Hz. The time window for fast Fourier transform is of size 0.06 s, which corresponds to the travel time through the reservoir having thickness of about 30–70 m with the P-wave velocity of 2500 m/s. Each window was tapered from each side using a Hanning taper and the spectra were smoothed with a five point median filter.

TESTS ON SYNTHETIC DATA

Before showing the results of the time-lapse estimates of the attenuation from the field data, we first examine the robustness and the accuracy of the 4DRSM with different noise distributions using a synthetic model. To this end, we create a simple model with two reflectors: one above the reservoir and one below the reservoir. We propagate a wavefield from a source which is located 10 m below the surface (see Fig. 11) with a peak frequency of 22.5 Hz. The single receiver recording the
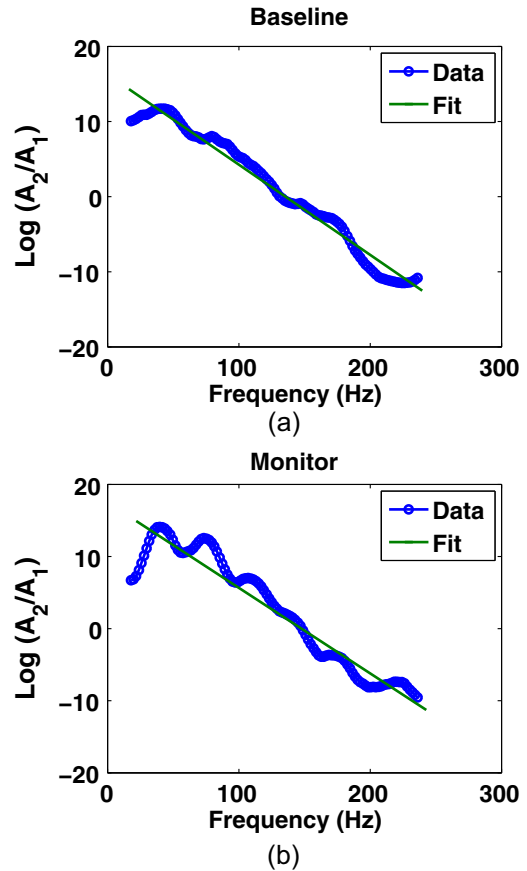

Figure 10 Logarithm of spectral ratio of data in time window t_2 to that in t_1 (shown in Figure 8) as a function of frequency: (a) baseline and (b) monitor.
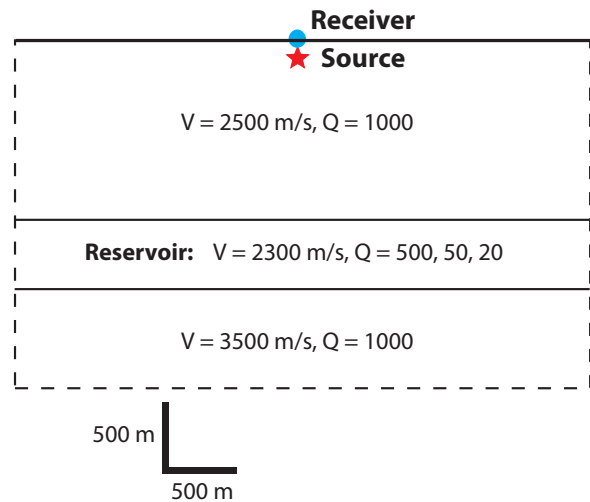

Figure 11 Schematic of the geometry of the synthetic test.

signal is located at the surface and at the same horizontal position as the source. The velocity and Q-factor for each layer are given in Fig. 11. We conduct tests for three Q-factors of 500, 50, and 20 within the reservoir layer to test the accuracy of 4DRSM (see Fig. 11). The synthetic data are modeled with the discrete wavenumber domain method with a frequency-independent Q-factor (Bouchon 1981). This method is a 3D pseudo-analytical method that allows accurate modeling of the effects of attenuation while avoiding the effects of numerical dispersion typical for numerical propagators such as finite difference or finite element.

In Fig. 12, we show three seismic traces obtained for the models with three different reservoir Q-factors (500, 50, and 20) where traces in Fig. 12(a) are noise-free, and those in Fig. 12(b) have been contaminated with additive Gaussian noise. The Gaussian noise has zero mean and a standard deviation of 10% of the maximum amplitude. The arrival times at 1.38 s and 1.78 s (in Fig. 12) correspond to the reflections from the horizons above and below the reservoir, respectively. We define a window size of 0.3 s with a Hanning taper (e.g., Oppenheim and Schafer 2010, pp. 536) at each end. The windows t_1 and t_2 are centred at each arrival time on the trace; we calculate the amplitude spectra for each window. The size of the taper is 30 % of the window size. Figure 13 shows the spectra for each arrival time with and without noise.

The variation in Q within the reservoir layer affects not only the amplitudes of the signal at t_2 but also has a slight effect on the signal at t_1 (see the increase in amplitude at 1.38 s in Fig. 12(a) and spectra magnitude in Fig. 13 when the reservoir Q value decreases from 500 to 20). We also observe that amplitude at t_2 is phase shifted when Q is reduced. This effect is caused by velocity dispersion: velocity in attenuative media must be frequency and Q-factor dependent in order to satisfy signal causality (Aki and Richards 2002, pp. 165-177). This affects the reflectivity through impedance and changes the reflected signal (amplitude and phase) from above and below the reservoir based on the reservoir Q-factor.

After taking the ratio of the spectra and then the logarithm, we estimate the slope to find Q. Figure 14 shows the logarithm of spectral ratios and their fit for noise-free and for noisy data. We observe that the fits for Q-factors of 20 and 50 are more accurate than those for 500 regardless of the noise. This is because high Q-factors give flatter logarithm of spectral ratios; thus, the slope is more sensitive to small variations in the spectra. Nevertheless, the fit for a Q-factor of 500 is still within a 10 % error. Although clearly there are many other sources of error that are not investigated here, these observations indicate that the estimation of the Q-factor is robust
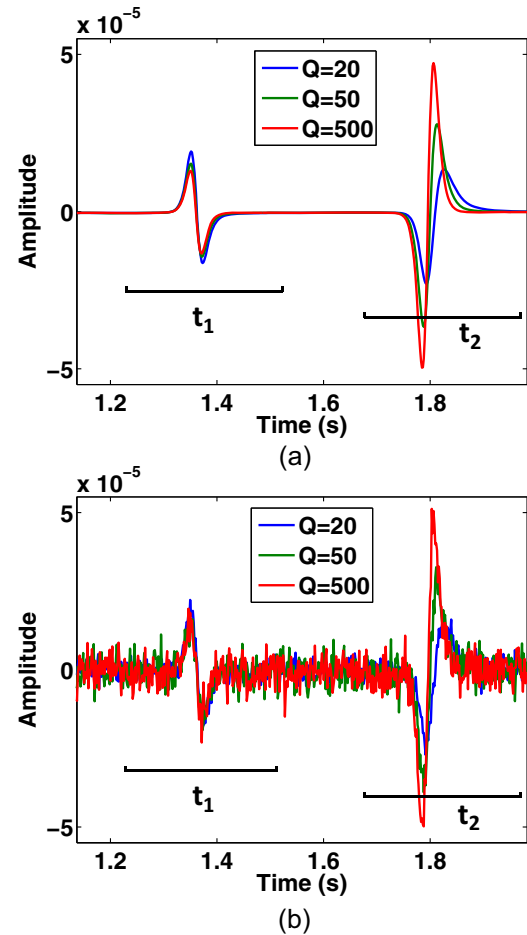

Figure 12 Three seismic traces generated with different Q-factors within the reservoir layer (500, 50, and 20) shown in the schematic geometry in Fig. 11: (a) without noise and (b) with added Gaussian noise with zero mean and standard deviation of 10% of the maximum amplitude. The time windows at t_1 and t_2 correspond to the reflections from the reflections from above and below the reservoir, respectively. Note that the dispersion effect from above and below the reservoir is considered inside the time window.

giving us the confidence to apply 4DRSM to the time-lapse field data.

FIELD DATA RESULTS - APPLICATION OF 4D-RELATIVE SPECTRUM METHOD

We now apply the method to the time-lapse 3D seismic data set using a single trace, from each pre-stack time-migrated gather, corresponding to the smallest offset, which is 16 m. We use a time window of size 0.06 s tapered at the beginning and end using a Hanning taper over 30 % of the window size. This time window was selected to be approximately the
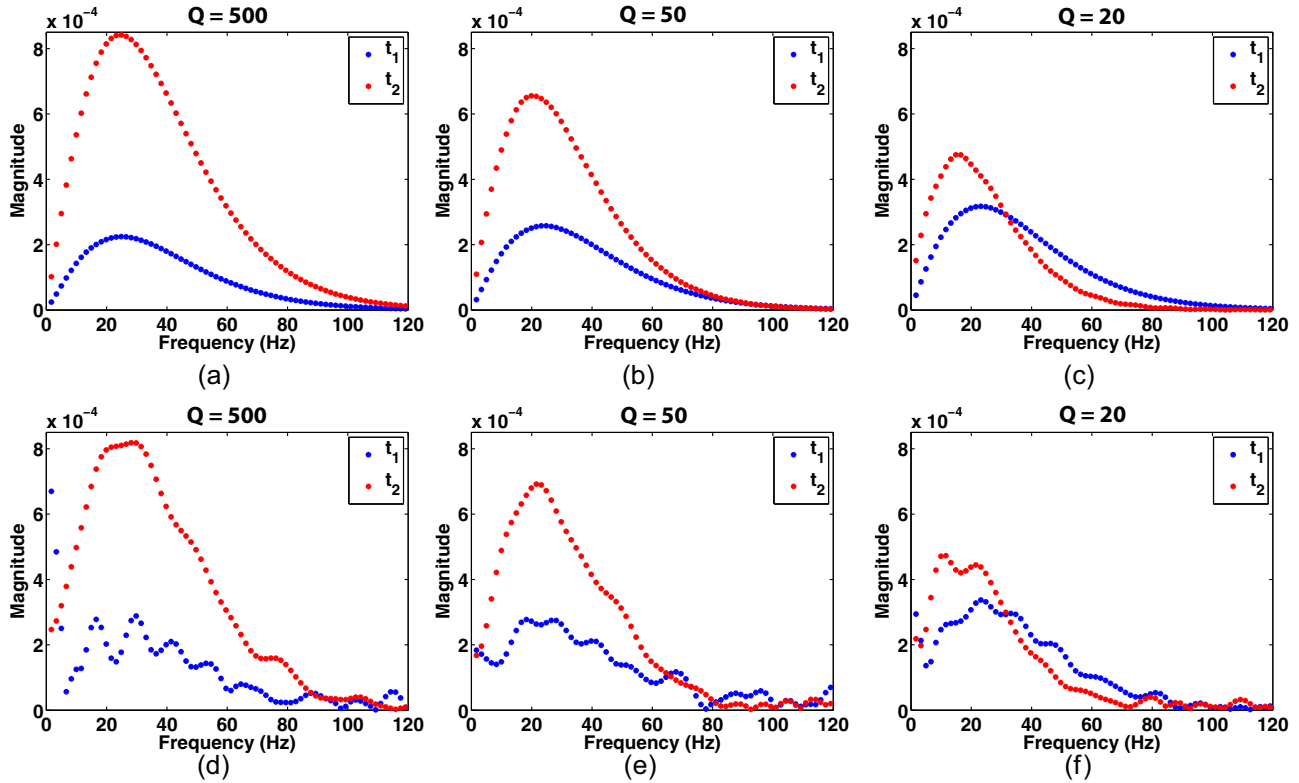
Figure 13 Amplitude spectra, as a function of frequency, of the windowed trace around the times that correspond to above ($t_1 = 1.38$ s) and below ($t_2 = 1.78$ s) the reservoir with different reservoir Q-factors of 500, 50, and 20: (a)–(c) without noise and (d)–(f) with added Gaussian noise with zero mean and standard deviation of 10% of the maximum amplitude. Note that the magnitude scale (the vertical axis) of the each plot is the same. Note also that the magnitudes above the reservoir are also affected by velocity dispersion.

two-way propagation time through the 60–70 m thick reservoir whose velocity is 2500 m/s (see well logs in Fig. 1). Windows of smaller size were also tested and showed similar results as long as they sufficiently sampled the same frequency range. However, the time window of 0.01 s used for time-lapse amplitude and time-shift calculations in Fig. 7 were not large enough to provide adequate sampling of the frequency range that is necessary for our analysis. The calculated spectra from each time window was smoothed by a five-point median filter to reduce noise. During the estimation of the relative spectra, the windows at t_1 were not overlapping with windows at t_2 to prevent frequency tuning effects that may cause notches in the spectra. We also evaluated the similarity of the spectra from windows at t_1 (above the reservoir) between the baseline and monitor surveys. Although this is not a necessary condition for 4DRSM, as described above, it provides a measure of consistency between the two surveys. If the values of the slopes γ_1, calculated at t_1 from $\log(|A_1|) = -\gamma_1 f + \log(G_1)$, were not similar within 15%, we discarded the Q-estimates of

the reservoir and replaced them by averaging Q values from adjacent points; this was necessary for less than 5 % of all points.

Figure 15 illustrates the differential Q^{-1} (i.e., $Q_B^{-1} - Q_M^{-1}$), and its relative uncertainty $\frac{\delta(Q_B^{-1} - Q_M^{-1})}{(Q_B^{-1} - Q_M^{-1})}$, estimated by the 4DRSM with reference reflections at times $t_1 = 0.22$ s (a reflection from above the reservoir) and $t_2 = 0.4$ s (a reflection from below the reservoir), over the frequency range between 15 Hz and 200 Hz, chosen based on Figs. 9 and 10. The relative uncertainty was derived from the error bar of the fit, separately estimated for each data set ($\delta Q_B^{-1}, \delta Q_M^{-1}$). Figure 16 shows the differential Q-factor and its relative uncertainty calculated respectively as $(Q_M - Q_B)$ and $\frac{\delta(Q_M - Q_B)}{Q_M - Q_B}$ (i.e., $\frac{Q_M^2 \delta Q_M^{-1} + Q_B^2 \delta Q_B^{-1}}{Q_M - Q_B}$). The relative uncertainties (shown in Figs. 15(b) and 16(b)) are uncorrelated with the geometry of the SAGD wells and show values below 15% and 20%, respectively. To verify that the observed differences in Figures 15(a) and 16(a) indeed correspond to reservoir changes and not to the reflectors above it, two control results were calculated by
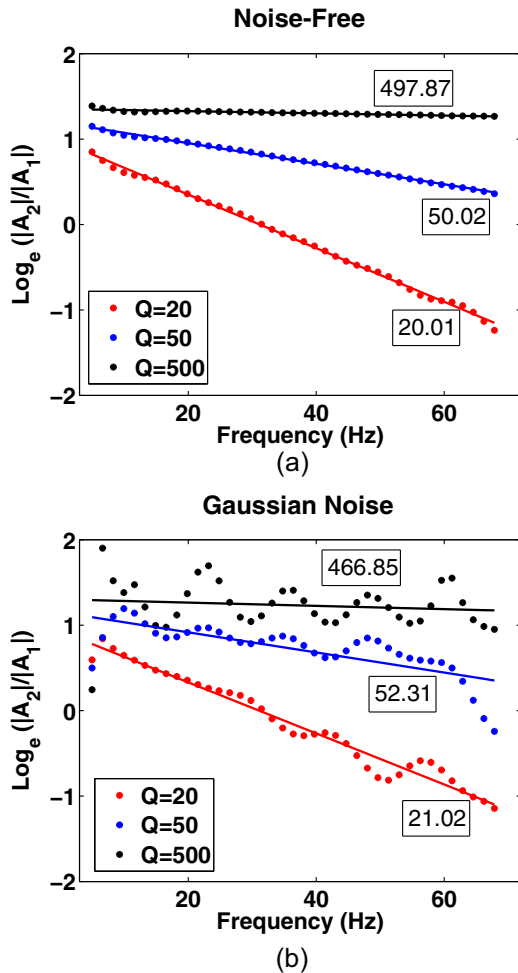
Figure 14 The logarithm of spectral ratios and their fit as a function of frequency estimated from the amplitude spectra given in Fig. 13 for different reservoir Q-factors (20, 50, and 500): (a) without noise, and (b) with added Gaussian noise with zero mean and standard deviation of 10% of the maximum amplitude. Values of Q found from the slopes are shown in black boxes for each spectral ratio.

Figure 15 Differential Q^{-1} $(Q_B^{-1}\text{-}Q_M^{-1})$ (a) and its uncertainty (b) between the baseline and the monitor data sets that were estimated using the 4DRSM using 0.06 s windows centered at time $t_1 = 0.22$ s and time $t_2 = 0.4$ s. Black lines indicate the position of the wells through which the reservoir is heated.

4DRSM with different reference reflectors. These are illustrated in Fig. 17 for the differential Q^{-1}, and in Fig. 18 for the differential Q. Figures 17(a) and 18(a) correspond to reference reflectors at $t_1 = 0.17$ s and $t_2 = 0.4$ s, whose comparison with Figs. 15(a) and 16(a) illustrate fairly good reproducibility. Conversely, Figs. 17(b) and 18(b) were calculated with reflectors at times $t_1 = 0.17$ s and $t_2 = 0.22$ s, with both times corresponding to the region above the reservoir; here we do not observe any alignment along the SAGD wells. Therefore, we conclude that the observed changes in Figs. 15(a), 16(a), 17(a), and 18(a) are most likely caused by changes in the reservoir.
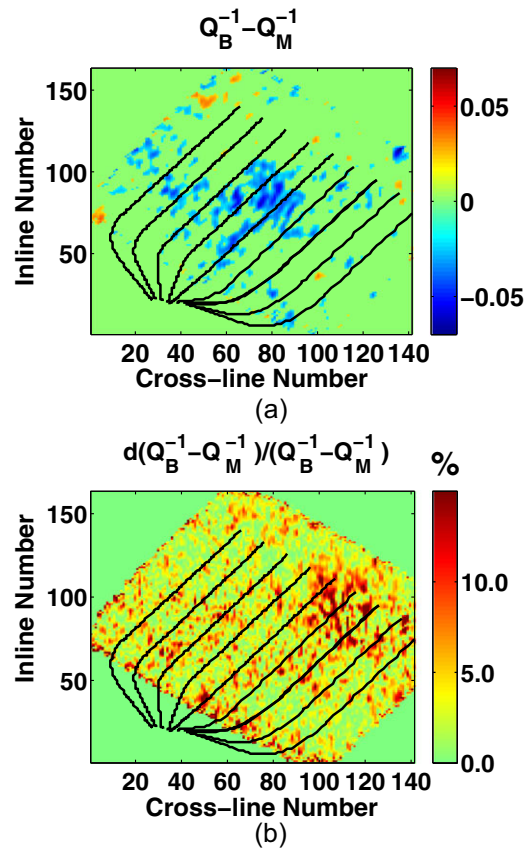
Although spatial maps of differential Q^{-1} and Q factors exhibit an alignment along the SAGD wells, as did the results of the standard 4D (time-lapse) analysis for amplitude changes, shown in Fig. 7(a), the interpretation of the three sets of results are different. The discussion and interpretation of the observed differences between Q and Q^{-1} factors are left for the next section. The difference between the changes in Q and in the 4D amplitudes is explained by different timescales at which the change is monitored. Time-lapse amplitude (and time-shift) measurements use a relatively small time window and thus monitor small-scale anomalies. This analysis depends strongly on data repeatability and matching (both amplitudes and spectra) between the time-lapse data sets and is prone to suffer from cycle skipping. In contrast, 4DRSM estimates a larger scale change by using a larger time window to
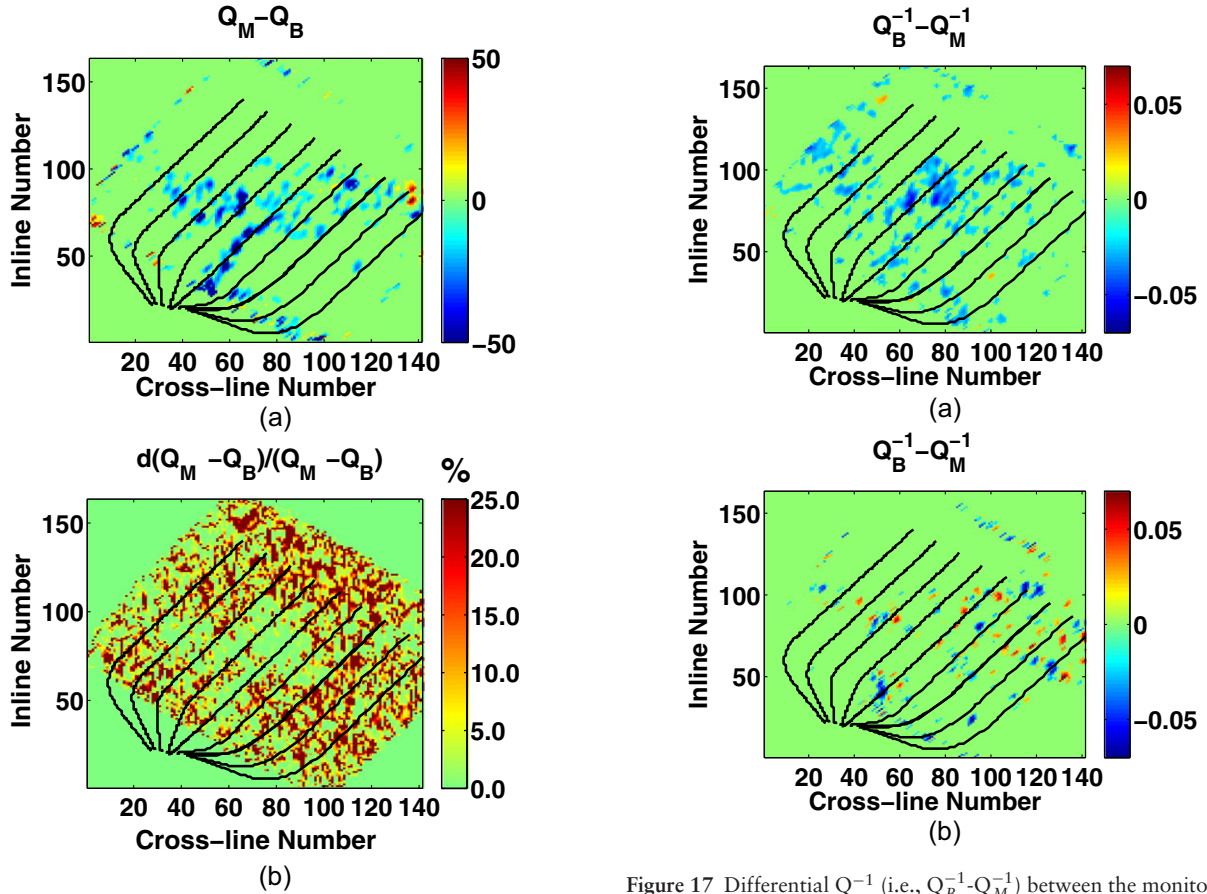
Figure 16 Differential Q-factor ($Q_M - Q_B$)(a) and its uncertainty (b) between the monitor and the baseline data sets that were estimated using a 4DRSM with the same times t_1 and t_2 as in Fig. 15. Black lines indicate the position of the SAGD wells.

Figure 17 Differential Q^{-1} (i.e., Q_B^{-1}-Q_M^{-1}) between the monitor and the baseline data sets that were calculated as control tests. The result (a) was calculated with times $t_1 = 0.17$ s and $t_2 = 0.4$ s, and (b) with times $t_1 = 0.17$ s and $t_2 = 0.22$ s. Black lines indicate the position of the SAGD wells.

adequately sample the spectrum. Moreover, 4DRSM measures a relative change (i.e., the difference in the spectral ratios, which compares signals reflected from above and below the reservoir within each survey), and thus it is less sensitive to preprocessing steps, as described above. We also tested the changes in amplitude and time-shift using the same time window size as was used for Q estimation. However, these estimates showed no correlation with the injection wells, which is likely because they included too large a portion of signal that did not change between the surveys. The goal of this study is to focus on the dependence of attenuation on viscosity and as the amplitude (and time-shift) change information does not provide a direct relationship with viscosity changes, their interpretation will not be further discussed.

VISCOSITY CHANGES

In order to relate the results obtained in Figs. 15 and 16 with the physics of the changes within reservoir, particularly with the viscosity, we need to review the viscoelastic mechanism of heavy oils, which corresponds to the empirical predictions of the Cole–Cole model for complex shear modulus (see e.g., Batzle *et al.* 2006b; Behura *et al.* 2007; Das and Batzle 2008). However, this model does not give a simple relationship between the Q-factor and the viscosity. We instead consider two models with a linear relationship between Q and viscosity, each of which behaves like the Cole–Cole model in a different frequency range (see Fig. 19). The first model is the Kelvin–Voigt model, which matches the Cole–Cole model at frequencies lower than the relaxation frequency and corresponds to
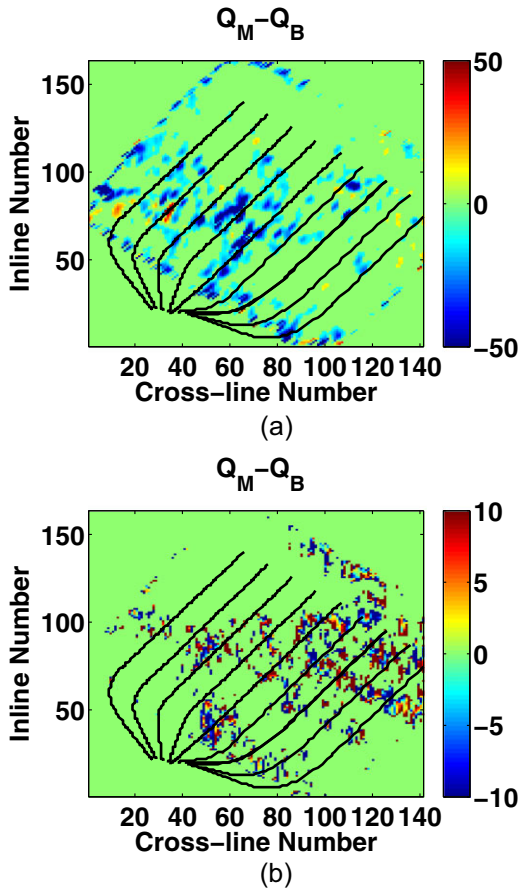
QM−QB

(a)

QM−QB

(b)

Figure 18 Differential Q-factor between the monitor and baseline data sets calculated as control tests. The result in (a) was calculated with times $t_1 = 0.17$ s and $t_2 = 0.4$ s, and that in (b) with times $t_1 = 0.17$ s and $t_2 = 0.22$ s. Black lines indicate the position of the SAGD wells.
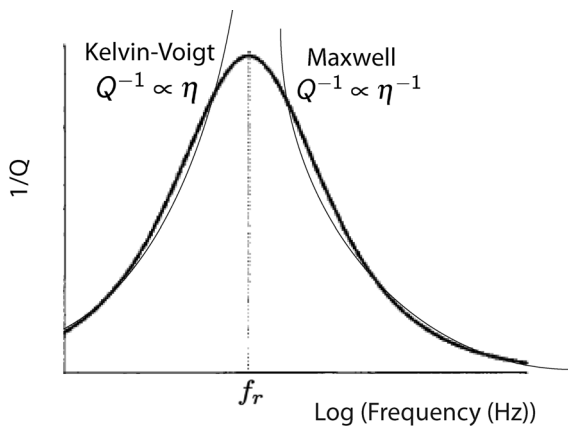

Figure 19 Schematic for the Cole–Cole viscoelastic model (dark line) where Kelvin–Voigt and Maxwell viscoelastic models occupy different frequency ranges; f_r corresponds to the relaxation frequency and η to viscosity.

the state when the heavy oil is relaxed, in equilibrium, and has low viscosity. Maxwell, the second model, predicts the behavior of the unrelaxed oil at frequencies higher than the relaxation frequency and has high viscosity. More details about the relationship between viscosity and the relaxed/unrelaxed state can be found in e.g., (Batzle *et al.* 2006b).

Since we used a narrow frequency range for our analysis of the field data, we do not know which of the two models will best describe our data, and we do not know the precise frequency response of the heavy oil from the monitored reservoir (i.e., we do not know whether the frequency range of our estimates is bigger or smaller than the relaxation frequency). Therefore, we assessed the viscosity predicted by both models. Note that this approximation should be valid for any relaxation coefficients of the Cole–Cole model.

The Q-factor in the Kelvin–Voigt viscoelastic model is given by $Q(f) = \frac{\rho c_0^2}{2\pi f \eta}$ (e.g., Carcione 2007 pp. 72), where f, ρ, c_0, and η are the frequency, density, wave velocity, and viscosity of the medium, respectively. This model has almost the same Q-factor representation as that of a pure viscous fluid, given by $Q(f) = \frac{3\rho c_0^2}{8\pi f \eta}$ (e.g., Mavko *et al.* 1998, pp. 213), suggesting that the Kelvin–Voigt model resembles the behavior of a viscous fluid.

From the Q-factor, we can find the viscosity by $\eta = \frac{\rho c_0^2}{2\pi f} Q^{-1}$, or in differential form as

$$\Delta \eta = \frac{\rho c_0^2}{2\pi f} \Delta Q^{-1}. \tag{9}$$

The Q-factor in the Maxwell model is given by $Q(f) = \frac{2\pi f \eta}{\rho c_0^2}$ (e.g., Carcione, 2007 pp. 71), from which we obtain the viscosity by $\eta = \frac{\rho c_0^2}{2\pi f} Q$, or in differential form as

$$\Delta \eta = \frac{\rho c_0^2}{2\pi f} \Delta Q. \tag{10}$$

The relationship between Q-factors and viscosity η in the Maxwell and Kelvin–Voigt models are reciprocal.

Because we do not posses well-log information after the steam injection, we assume constant (or nearly constant) values for reservoir density $\rho = 2050$ kg/m^3 and P wave velocity $c_0 = 2500$ m/s, taken from the baseline well logs (Fig. 1). Using the average frequency over which we estimated the Q-factor, i.e., $f = \frac{15+200}{2}$ Hz, we calculate the difference in viscosity $\Delta \eta$ for both the Kelvin–Voigt and Maxwell models, given in Fig. 20. Note that, although the velocity and density of heavy oil with temperature might change (i.e., an expected change from laboratory measurements is about 30 % for velocity and 10 % for density (Batzle *et al.* 2006a; Mochinaga *et al.*,
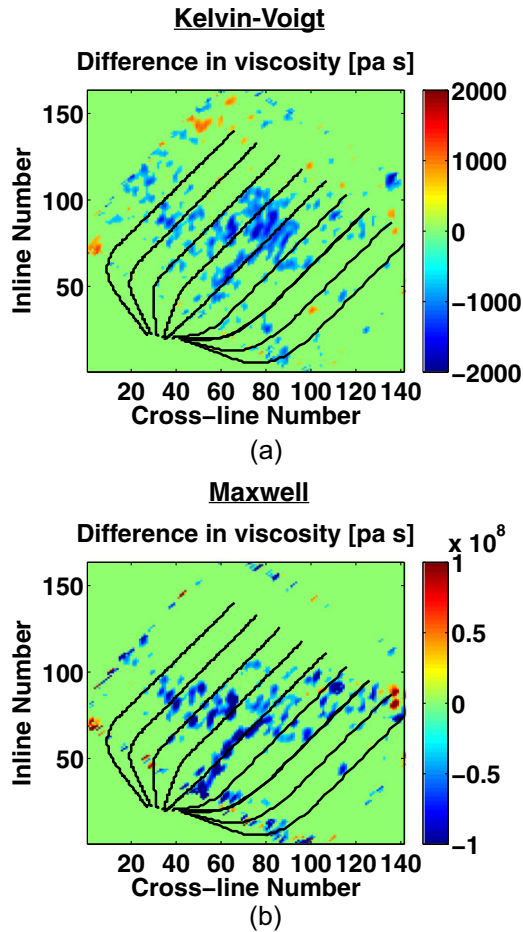
Kelvin-Voigt

Difference in viscosity [pa s]

(a)

Maxwell

Difference in viscosity [pa s]

(b)

Figure 20 Difference in viscosity between the heated and the in-situ heavy oil that was calculated by equation (9) for Kelvin–Voigt model (a) and by equation (10) for Maxwell model (b).

2006)), this change is expected to be minor, compared with that in the viscosity. The variation in viscosity is expected to have approximately double logarithmic behavior (Batzle *et al.* 2006a).

From Fig. 20, we observe that the variations in viscosity calculated with the Kelvin–Voigt viscoelastic model are more realistic (changes within the range of 2000 Pa·s) than those for the Maxwell model (changes within the range of 10^8 Pa·s) because the viscosity of heavy oil is expected to be between 1000 Pa·s and 5000 Pa·s. This indicates that heavy oil is in the relaxed state, described above, where the heated oil is melted enough to flow through the reservoir. As discussed above, the possible variation in velocity and density should not have large impact on the estimates for viscosity changes as they have the same dependence between $\Delta\eta$ and ΔQ^{-1} in equation (9), and ΔQ in equation (10). Thus, we expect to have similar un-

certainty estimates for viscosity changes as these estimated in Fig. 15(b) and 16(b). Additional information such as injection rates, temperatures, pressures, saturation, and permeability variations would improve our understanding of the physics of the reservoir.

CONCLUSIONS

In this study, we investigated the effect of steam injection into a heavy oil reservoir on seismic attenuation. We showed that, within the seismic frequency band, the attenuation at seismic frequencies due to heavy oils can be measured using a frequency-independent Q-factor. To measure the attenuation, we adapted the spectral ratio method into 4D-RELATIVE SPECTRUM METHOD for monitoring target-oriented time-lapse Q-factor changes from surface reflection seismic data. We tested the 4DRSM for robustness and accuracy without noise and with additive Gaussian noise, and applied it to data from a heavy oil field in Athabasca, Canada. We illustrated that changes in Q^{-1} and Q can be related to viscosity changes through the viscoelastic behavior of the Kelvin–Voigt and Maxwell models. We also showed that for these data the Kelvin–Voigt model explains the detected changes better than the Maxwell model. These results provide a quantitative measure of viscosity changes and improve the monitoring process of the heating of the reservoir.

REFERENCES

Aki K. and Richards P.G. 2002. *Quantitative seismology*. Univ Science Books.

Badri M. and Mooney H.M. 1987. Q measurements from compressional seismic waves in unconsolidated sediments. *Geophysics* **52**, 772–784.

Barson D. 2001. Flow systems in the Mannville Group in the east-central Athabasca area and implications for steam-assisted gravity drainage (SAGD) operations for in situ bitumen production. *Bulletin of Canadian Petroleum Geology* **49**, 376–392.

Batzle M., Hofmann R. and Han D.-H. 2006a. Heavy oil - seismic properties. *Leading Edge* **25**, 750–757.

Batzle M., Han D.-H. and Hofmann R. 2006b. Fluid mobility and frequency-dependent seismic velocity - Direct measurements. *Geophysics* **71**, N1–N9.

Behura J., Batzle M. Hofmann R. and Dorgan J. 2007. Heavy oils: Their shear story. *Geophysics* **72**, E175–E183.

Blanchard T., Clark R. van der Baan M. and Laws E. 2009. Time-lapse attenuation as a tool for monitoring pore fluid changes in hydrocarbon reservoirs. Presented at the 71st EAGE Conference & Exhibition.

Bouchon M. 1981. A simple method to calculate Green's functions for elastic layered media. *Bulletin of the Seismological Society of America* **71**, 959–971.

Byerley G., Barham G., Tomberlin T. and Vandal B. 2008. 4D seismic monitoring applied to SAGD operations at Surmont, Alberta, Canada. 78th SEG meeting, Las Vegas, NV, Expanded Abstracts, 3959–3963.

Carcione J. M. 2007. *Wave Fields in Real Media - Wave Propagation in Anisotropic, Anelastic, Porous and Electromagnetic Media.* Elsevier.

Carter A. 2003. *Seismic wave attenuation from surface seismic reflection surveys - an exploration tool.* University of Leeds PHD thesis.

Chen Q. and Sidney S. 1997. Seismic attribute technology for reservoir forecasting and monitoring. *The Leading Edge* **16**, 445–448.

Chopra S. 2010. Heavy oils. *reservoir characterization and production monitoring.* Society of Exploration Geophysicists.

Clark B., Graves W. G., Lopez-de-Cardenas J. E., Gurfinkel M. E. and Peats A. W. 2007. Working Document of the NPC Global Oil and Gas Study, Topic Paper **22**.

Clark R.A., Benson P.M., Carter A.J. and Moreno C.A.G. 2009. Anisotropic p-wave attenuation measured from a multi-azimuth surface seismic reflection survey. *Geophysical Prospecting* **57**, 835–845.

Cole K.C. and Cole H.R. 1941. Dispersion and Absorbtion in Dielectrics. *Journal of Chemical Physics* **9**, 341–351.

Das A. and Batzle M. 2008. Modeling studies of heavy oil - in between solid and fluid properties. Leading Edge *Special Section: Heavy oil*, 1116–1123.

Dasgupta R. and Clark R.A. 1998. Estimation of Q from surface seismic reflection data. *Geophysics* **63**, 2120–2128.

Eastwood L. 1993. Temperature-dependent propagation of P- and S-waves in Cold Lake oil sands: Comparison of theory and experiment. *Geophysics* **58**, 863–872.

Feustel A.J. and Young R.P. 1994. Q_β estimates from spectral ratios and multiple lapse time window analysis: results from an underground research laboratory in granite. *Geophysical research letters* **21**, 1503–1506.

Han D.-H., Liu J. and Batzle M. 2007. Shear velocity as the function of frequency in heavy oils. 77th SEG Abstract 1716–1719.

Hauge P.S. 1981. Measurements of attenuation from vertical seismic profiles. *Geophysics* **46**, 1548–1558.

Hedlin K., Mewhort L. and Margrave G. 2001. Delineation of steam flood using seismic attenuation. 71st SEG meeting, Expanded Abstracts, 1572–1575.

Kendall R. 2009. Using time lapse seismic to monitor the THAI heavy oil production process. 79th SEG meeting, Expanded Abstracts, 3954–3958.

Kragh E. and Christie P. 2002. Seismic repeatability, normalized rms, and predictability. *The Leading Edge* **21**, 640–647.

Lecerf D., Rogers M. and Lefeuvre F. 2006. Time-spectral analysis for 4D data q-controlled calibration. Presented at the 68th EAGE Conference & Exhibition.

Mateeva A.A. 2003. Thin horizontal layering as a stratigraphic filter in absorption estimation and seismic deconvolution. PhD thesis, Colorado School of Mines.

Matsushima J. 2006. Seismic wave attenuation in methane hydrate-bearing sediments: vertical seismic profiling data from the Nankai trough exploratory well, offshore Tokai, central Japan. *Journal of Geophysical Research* **111**, B10101.

Mavko G., Mukerji T. and Dvorkin J. 1998. *The Rock Physics Handbook.* Cambridge University Press.

Menke W., Levin V. and Sethi R. 1995. Seismic attenuation in the crust at the mid-Atlantic plate boundary in south-west Iceland. *International Journal of Geophysics* **122**, 175–182.

Mochinaga H., Onozuka S., Kono F., Ogawa T., Takahashi A. and Torigoe T. 2006. Properties of Oil sands and Bitumen in Athabasca. CSPG-CSEG-CWLS Convention, 39–44.

Oppenheim A.V. and Schafer W.R. 2010. Discrete-Time Signal Processing 3rd ed. Pearson.

Reine C., Clark R. and van der Baan M. 2012. Robust prestack Q-determination using surface seismic data: Part 1- method and synthetic examples. *Geophysics* **77**, R45–R56.

Reine C., Clark R. and van der Baan M. 2012b. Robust prestack Q-determination using surface seismic data: Part 2-3D case study. *Geophysics* **77**, B1–B10.

Reine C., van der Baan M. and Clark R. 2009. The robustness of seismic attenuation measurements using fixed-and variable-window time-frequency transforms. *Geophysics* **74**, WA123–WA135.

Rickett J. 2006. Integrated estimation of interval-attenuation profiles. *Geophysics* **71**, A19–A23.

Schmitt D. 1999. Seismic attributes for monitoring of a shallow heated heavy oil reservoir: a case study. *Geophysics* **64**, 368–377.

Sun S. and Castagna J.P. 2000. Attenuation estimation from vertical seismic profile data. Presented at the 2000 SEG Annual Meeting.

Toksöz M.N., Johnston H.D. and Timur A. 1979. Attenuation of seismic waves in dry and saturated rocks: I. laboratory measurements. *Geophysics* **44**, 681–690.

Vasconcelos I., and Jenner E. 2005. Estimation of azimuthally varying attenuation from surface seismic data. Center for Wave Phenomena Annual Report CWP-516, 89–106.

Vendati N. and Sen K.M. 2009. Seismic inversion tracks in situ combustion: A case study from Balol oil fiel, India. *Geophysics* **74**, B103–B112.

Wang Y. 2003. Quantifying the effectiveness of stabilized inverse Q filtering. *Geophysics* **68**, 337–345.

APPENDIX: DERIVATION OF THE RELATIVE Q-FACTOR

The derivation of the Q-factor between two arrival times (two reflectors), i.e., t_1 and t_2, is carried out with the assumption that the Q-factor is constant within a frequency

band, and thus from equation (5) for, times t_1 and t_2, we obtain

$$\gamma_1 = \frac{\pi t_1}{Q} \text{ and } \gamma_2 = \frac{\pi t_2}{Q}. \tag{A1}$$

Assuming that the waves propagate along a stationary path (i.e., the wave path from the source (t = 0) to time t_1 is part of the wave path from the source to time t_2), we take the difference between γ_2 and γ_1

$$\gamma_2 - \gamma_1 = \frac{\pi}{Q}(t_2 - t_1). \tag{A2}$$

The Q value in equation A-2 is given between times t_2 and t_1 and does not depend on the Q from above time t_1 as long as the initial assumption of stationary path is satisfied. Note however that with reflection seismic data where waves propagate a two-way path (i.e., from a source down to the reflectors at times t_1 and t_2, and up toward a receiver), this assumption is satisfied only with zero- or small-offset traces and does not hold when large-offset traces are used in the Q estimation. To account for the two-way path, we add a factor $\frac{1}{2}$ to eq. A-2, and obtain eq. 8.